EDGE ARTICLE

Check for updates

A rationally designed two-dimensional MoSe2/Ti2CO2 heterojunction for photocatalytic overall water splitting: simultaneously suppressing electron–hole recombination and photocorrosion†

Cen-Feng Fu, Xingxing Li [ID] and Jinlong Yang [ID]*

Electron–hole recombination and photocorrosion are two challenges that seriously limit the application of two-dimensional (2D) transition metal dichalcogenides (TMDs) for photocatalytic water splitting. In this work, we propose a 2D van der Waals MoSe2/Ti2CO2 heterojunction that features promising resistance to both electron–hole recombination and photocorrosion existing in TMDs. By means of first-principles calculations, the MoSe2/Ti2CO2 heterojunction is demonstrated to be a direct Z-scheme photocatalyst for overall water splitting with MoSe2 and Ti2CO2 serving as photocatalysts for hydrogen and oxygen evolution reactions, respectively, which is beneficial to electron–hole separation. The ultrafast migration of photo-generated holes from MoSe2 to Ti2CO2 as well as the anti-photocorrosion ability of Ti2CO2 are responsible for photocatalytic stability. This heterojunction is experimentally reachable and exhibits a high solar-to-hydrogen efficiency of 12%. The strategy proposed here paves the way for developing 2D photocatalysts for water splitting with high performance and stability in experiments.

Introduction

Two-dimensional (2D) photocatalysts for water splitting have attracted significant attention due to their unique electronic and optical properties compared to traditional bulk materials.[1–6] The representative 2D MoS2 nanosheets of transition metal dichalcogenides (TMDs) have been demonstrated to be potential photocatalysts for overall water splitting.[7–10] The homogeneous distributions of photo-generated electrons and holes on the layers of 2D TMDs make both the hydrogen evolution reaction (HER) and oxygen evolution reaction (OER) proceed on the same surface. This results in electron–hole recombination, which reduces the energy conversion efficiency.[3] On the other hand, chalcogenide-based photocatalysts for water splitting suffer from the photocorrosion problem,[10,11] thus seriously restricting their practical usage. When photocorrosion occurs, the photo-generated electrons or holes will not participate in water decomposition, while resulting in the semiconductors themselves being reduced or oxidized, and leading to material disintegration.[12,13] For chalcogenide-based photocatalysts, photocorrosion results from the oxidation of the chalcogen components by the photo-generated holes.[11–13]

Hefei National Laboratory of Physical Science at the Microscale, Department of Chemical Physics, Synergetic Innovation Center of Quantum Information & Quantum Physics, University of Science and Technology of China, Anhui 230026, China. E-mail: jlyang@ustc.edu.cn

For instance, the previous reports suggested that the severe photocorrosion issue occurs in the edges as well as defect positions of MoS2 nanosheets.[14] Consequently, the electron–hole recombination and photocorrosion issues seriously limit the application of TMDs for photocatalytic water splitting.

For bulk photocatalysts, some rationally designed heterojunctions show effective inhibition of both electron–hole recombination[15–17] and photocorrosion[18–20] in experiments. As regards 2D TMDs for photocatalytic water splitting, constructing 2D type-II[21–24] and Z-scheme[25–28] heterojunctions has been reported to be effective in enhancing electron–hole separation. For these 2D heterojunctions, the OER proceeds relying on the chalcogen-containing materials and thus the photocorrosion situation is inevitable. To date, the challenge of addressing the photocorrosion problem in 2D chalcogenide-based photocatalysts has remained unsolved. It is urgent to find an avenue to simultaneously resist electron–hole recombination as well as photocorrosion issues for TMDs.

In this work, we propose that both the electron–hole recombination and photocorrosion phenomena in 2D TMDs are successfully suppressed *via* the rational design of 2D heterojunctions using a specific kind of semiconductor. This kind of semiconductor should hold these features: (1) the conduction band (CB) being slightly higher than the valence band (VB) of TMDs to achieve the ultrafast collection of the photo-generated holes from TMDs; (2) the band alignment being suitable for the OER, while TMDs serving as photocatalysts for the HER; (3) featuring the anti-photocorrosion ability to the photo-generated holes. Here, the

direct Z-scheme heterojunction is chosen due to its significant advantages compared to type-II and traditional Z-scheme heterojunctions with mediators.[29] By means of first-principles calculations, the 2D vdW heterojunction of $MoSe_2/Ti_2CO_2$ is demonstrated to be a good candidate. Ti_2CO_2 belongs to 2D materials of transition metal carbides (MXenes), which have been widely explored for energy storage and photoelectrocatalysis in experiments.[30–33] The 2D vdW heterojunctions can be easily prepared through mixing the dispersions of the two components according to the experimental reports.[34–36] The band structures reveal that this heterojunction is a direct Z-scheme photocatalyst for overall water splitting with $MoSe_2$ and Ti_2CO_2 acting as the HER and OER photocatalysts, respectively, which is beneficial for electron–hole separation. Non-adiabatic molecular dynamics (NAMD) simulations indicate that more than 65% of the photo-generated holes migrate from $MoSe_2$ to Ti_2CO_2 within 0.5 ps, which significantly reduces the probability of photocorrosion occurring in $MoSe_2$. Further studies on the free energy along the catalytic reaction routes show that the OER can occur spontaneously on the surface of Ti_2CO_2. Meanwhile, the Ti_2CO_2 material itself can suppress photocorrosion and its surface oxygen will not be oxidized by photo-generated holes. Moreover, it is worth mentioning that the theoretically predicted solar-to-hydrogen (STH) efficiency of this heterojunction is up to 12%, exceeding the requirement for 10% STH efficiency for practical applications.[37]

Results and discussion

The calculated lattice parameters of the $MoSe_2$ and Ti_2CO_2 monolayers are 3.32 and 3.03 Å, respectively, which are in agreement with the previously reported results.[25–27,38,39] A $\sqrt{13} \times \sqrt{13}$ super cell for $MoSe_2$ and a 4×4 super cell for Ti_2CO_2 are employed to construct the 2D vdW heterojunction with a lattice constant of 12.04 Å, which ensures that the lattice mismatches for both $MoSe_2$ and Ti_2CO_2 are within 1%. The configurations of the $MoSe_2/Ti_2CO_2$ heterojunction with different stacking patterns are examined (Fig. S1†). It is found that the effect of different stacking patterns on the binding energy and vertical distance between the two components of the heterojunction is negligible (Table S1†). The configuration (shown in Fig. 1(a)) with the largest binding energy is used for the following calculations. For this configuration, the vertical distance between $MoSe_2$ and Ti_2CO_2 is 3.07 Å and their binding energy is confirmed to be -16.8 meV per atom (-15.9 meV Å^{-2}), suggesting the presence of weak vdW interactions in the $MoSe_2/Ti_2CO_2$ heterojunction. This binding energy is comparable to that (-30 meV Å^{-2}) of a 2D black phosphorus/$BiVO_4$ heterojunction,[40] which has been fabricated as a direct Z-scheme photocatalyst for water splitting in the experiment through a solution mixing method.[34] Solution mixing is simple and low-cost to experimentally fabricate 2D vdW heterojunctions, including 2D direct Z-scheme photocatalysts of aza-CMP/C_2N[35] and α-Fe_2O_3/g-C_3N_4.[36] Except for the solution mixing method, there are other protocols for fabricating 2D vdW heterojunctions in experiments, including mechanical transfer and direct growth.[41,42] The stability of this heterojunction in water environments is examined by *ab initio* molecular dynamics (AIMD) simulations. The results reveal that the whole system reaches equilibrium after 4 ps and there is no structural
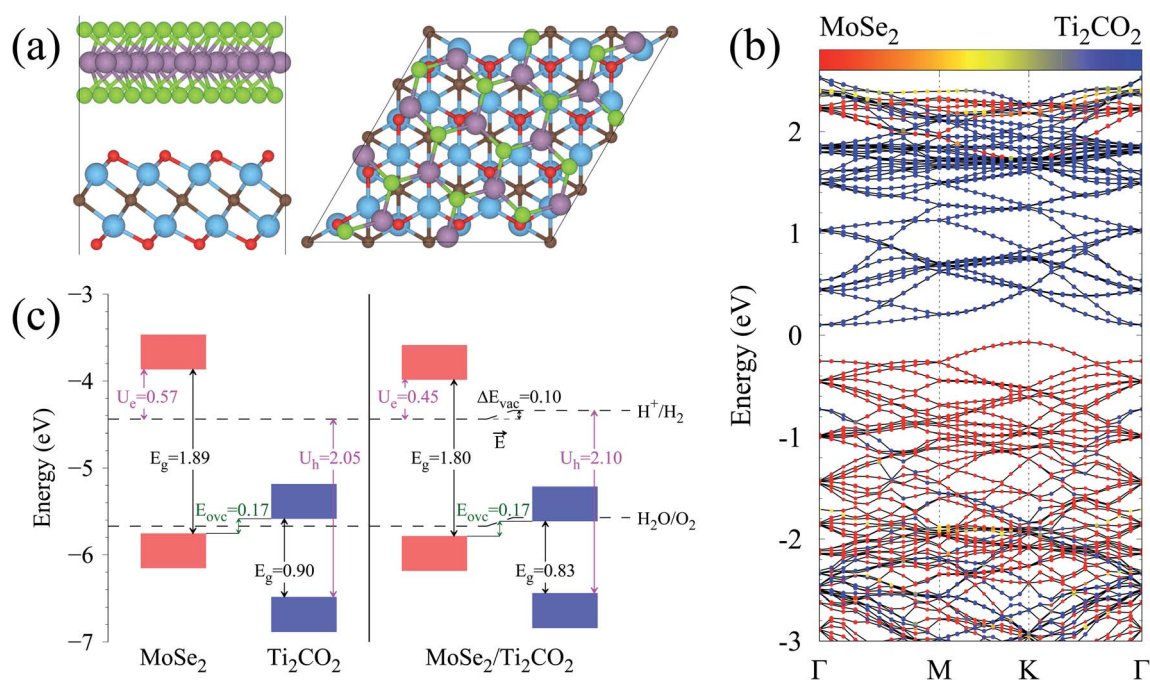
Fig. 1 (a) Side and top views of the $MoSe_2/Ti_2CO_2$ heterojunction with Mo, Se, Ti, C and O atoms represented as purple, green, cyan, brown and red balls, respectively. (b) Band structure of the $MoSe_2/Ti_2CO_2$ heterojunction. The Fermi level is set to zero. The circles with colors from red to blue represent the dominant contributions varying from $MoSe_2$ to Ti_2CO_2. (c) Band edge alignments of the free-standing $MoSe_2$ and Ti_2CO_2 monolayers as well as the $MoSe_2/Ti_2CO_2$ heterojunction. The values are all in eV.

disorder for the heterojunction nor reactions of the surface H_2O molecules on the heterojunction during the whole 10 ps simulation (Fig. S2†). Thus, it is confirmed that the $MoSe_2/Ti_2CO_2$ heterojunction is sufficiently stable in water.

The band structure of the $MoSe_2/Ti_2CO_2$ heterojunction calculated by the HSE06 hybrid functional is presented in Fig. 1(b). The band gap is 0.17 eV. The valence band maximum (VBM) appears at the K position mainly contributed by $MoSe_2$ and the conduction band minimum (CBM) arises at the Γ position mainly contributed by Ti_2CO_2. More detailed density of states (DOS) information can be seen in Fig. S4† and the spatial distribution of the VB and CB for the heterojunction is shown in Fig. S5.†

Fig. 1(c) illustrates the band edge alignments of the $MoSe_2$ and Ti_2CO_2 monolayers as well as their complex. The $MoSe_2$ monolayer features the CBM above the H_2/H_2O potential while the Ti_2CO_2 monolayer shows the VBM below the H_2O/O_2 potential. This indicates that the $MoSe_2$ and Ti_2CO_2 monolayers can serve as the HER and OER photocatalysts, respectively. The $MoSe_2/Ti_2CO_2$ heterojunction holds the same band edge alignment. Moreover, the CBM of Ti_2CO_2 is slightly higher than the VBM of $MoSe_2$ with an offset (E_{ovc}) of 0.17 eV, which benefits the photo-generated carriers rapidly migrating between the VB of $MoSe_2$ and the CB of Ti_2CO_2. Such a band edge alignment means that the $MoSe_2/Ti_2CO_2$ heterojunction is a direct Z-scheme photocatalyst for overall water splitting, which is favorable for electron–hole separation. The comparisons regarding the band edge alignments of the free-standing monolayers and the heterojunction in Fig. 1(c) reveal the variations for the band gaps of $MoSe_2$ and Ti_2CO_2 as well as U_e and U_h, which is ascribed to the interactions between the $MoSe_2$ and Ti_2CO_2 monolayers. Attributed to the larger work function of Ti_2CO_2 (5.66 eV) compared with $MoSe_2$ (4.48 eV), the charge redistribution phenomenon occurs (Fig. S6†) when these two kinds of monolayers contact each other. Bader charge analysis reveals that about 0.40 electron transfer from $MoSe_2$ to Ti_2CO_2 for the whole system. The corresponding electron transfer for $MoSe_2$ is only 0.03 per formula, indicating that the charge

transfer is weak. Therefore, the effect of charge transfer on the band structure is small and the dominant interaction between $MoSe_2$ and Ti_2CO_2 derives from the van der Waals interaction. Additionally, the charge redistribution brings about an electric field along the perpendicular direction pointing from $MoSe_2$ to Ti_2CO_2, thus leading to these two materials exhibiting different vacuum levels (representing by the ΔE_{vac} in Fig. 1(c)). The appearance of the vertical electric field is helpful with facilitating the recombination of the photo-generated holes in the $MoSe_2'$ VB and the photo-generated electrons in the Ti_2CO_2' CB. Simultaneously, both the undesired migrations of the photo-generated electrons from the $MoSe_2'$ CB to the Ti_2CO_2' CB and the photo-generated holes from the Ti_2CO_2' VB to the $MoSe_2'$ VB are well hindered. These are beneficial for the $MoSe_2/Ti_2CO_2$ heterojunction to facilitate photocatalytic water splitting by the Z-scheme mechanism.

The strain effects on the electronic structures of the $MoSe_2/Ti_2CO_2$ heterojunction have also been investigated (Fig. S7†). As strain varies from -2% to 2%, the band gap of $MoSe_2$ gradually decreases, while that of Ti_2CO_2 gradually increases. Within the whole strain change range, the $MoSe_2/Ti_2CO_2$ heterojunction keeps the suitable band edge alignment for Z-scheme photocatalytic water splitting. Additionally, the U_e and U_h values show an increasing trend with increasing strain, hinting that the compression strain is much more preferred for the $MoSe_2/Ti_2CO_2$ system to catalyze water decomposition.

The ultrafast migrations of the photo-generated carriers between the $MoSe_2'$ VB and the Ti_2CO_2' CB are further demonstrated by NAMD simulations.[43–45] According to the above discussion, the $MoSe_2'$ VB and the Ti_2CO_2' CB are chosen as the initial states for photo-generated holes and electrons, respectively, to explore interlayer and intralayer electron–hole recombination. As shown in Fig. 2(b), within 0.5 ps, more than 85% of the photo-generated holes recombine with electrons. Among them over 65% recombine with electrons in Ti_2CO_2 and only 20% belong to intralayer electron–hole recombination. Around 95% of the photo-generated electrons recombine with holes within 0.5 ps (Fig. 2(c)). The population for the interlayer
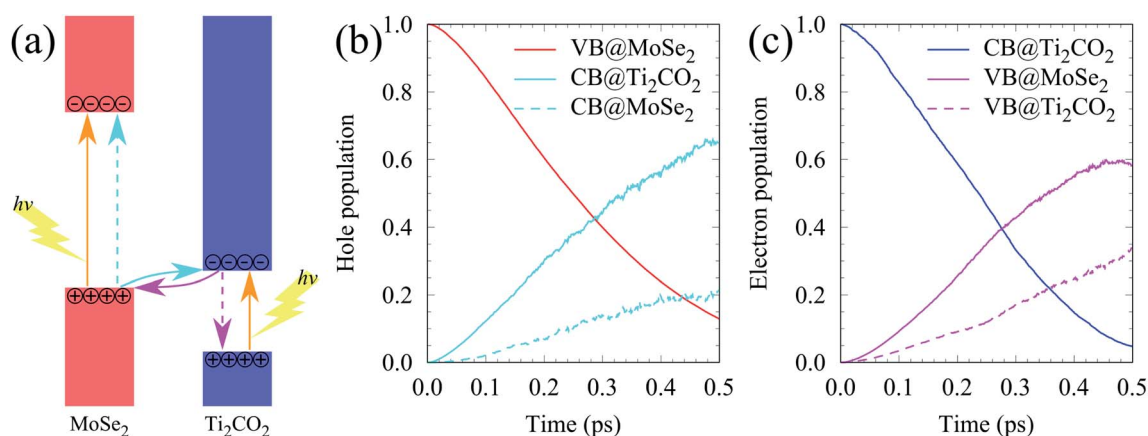

Fig. 2 (a) Schematic diagram of the photogenerated carrier transfer pathway for the $MoSe_2/Ti_2CO_2$ heterojunction. (b and c) The time dependent hole and electron population.

and intralayer electron–hole recombination is 60% and 35%, respectively. The NAMD simulations reveal that more than 65% of photo-generated holes transfer from $MoSe_2$ to Ti_2CO_2 within 0.5 ps, which greatly reduces the possibility of the Se components being oxidized by the photo-generated holes in $MoSe_2$, thereby being favorable of the elimination of photocorrosion.

The above studies have clearly implied that the $MoSe_2$/Ti_2CO_2 heterojunction has Z-scheme band edge alignment with ultrafast interlayer electron–hole recombination, which restricts photocorrosion arising in the $MoSe_2$ monolayer. The further examination of the photocatalytic activity and stability of Ti_2CO_2 is performed by investigating the free energy variations during the OER process. The OER is considered as a four-electron reaction process, where there are several intermediate states of *OH, *O, and *OOH absorbed on the material surface. In the first step, the H_2O molecule loses an electron–proton pair to form *OH. In the second step, *OH is oxidized to *O. In the third step, *O reacts with another H_2O molecule to yield *OOH. In the last step, *OOH releases an electron–proton pair and then desorbs from the material surface to achieve the production of the O_2 molecule. The various intermediate state configurations involved in the OER are presented in Fig. 3(a). The most stable absorbed H_2O molecule locates at the top of the Ti atom (Fig. S10†). For the structure of the absorbed *OH, the Ti atom moves up from the subsurface and bonds to the O atom of *OH after structural optimization. This Ti atom is the active site during the OER process. It stays on the surface and bonds to the adsorbed *O and *OOH. After the formation of the O_2 molecule (Fig. S11†), this Ti atom goes back to the subsurface and the surface of Ti_2CO_2 recovers. Fig. 3(b and c) reveal the free energy curves of the OER happening on the Ti_2CO_2' surface. It is found

that among the four procedures, the reaction for *O transforming into *OOH is the rate-determining step with free energy variation (ΔG) equal to 1.39 eV at pH = 7. By taking the extra potential provided by photo-generated holes into account, the ΔG of all four element reactions decrease (Fig. 3(b)), meaning that the whole OER can occur spontaneously from the viewpoint of energy. Albeit the pH value descends to 0 corresponding to strongly acid environments, the spontaneous OER process is still realized under light irradiation conditions (Fig. 3(c)). Additionally, we inspected the strain effects on ΔG during the OER process (Fig. S12†). The results reveal that the OER can proceed spontaneously *via* light illumination within a strain range of −2% to 2%.

To clarify the photocatalytic stability of Ti_2CO_2, we explore the reaction mechanism for Ti_2CO_2 oxidized by the photo-generated holes. For the Ti_2CO_2 monolayer, the Ti and C atoms are protected by the surface lattice O (O_L), so O_L will be oxidized by the photo-generated holes firstly. In the following content, ΔG for the OER process involving O_L of Ti_2CO_2 is investigated. Firstly, the reaction happens between O_L and the H_2O molecule to generate *OOH; Secondly, *OOH loses an electron–proton pair to form O_2, simultaneously leaving an O vacancy (V_O) on the material surface; Thirdly, the H_2O molecule releases an electron–proton pair at the V_O site to yield *OH; Finally, *OH releases an electron–proton pair to produce O_L (the intermediate state configurations corresponding to the reaction steps can be seen in Fig. 4(a)). As presented in Fig. 4(b), at pH = 0, both the first and second steps exhibit rather large ΔG, attaining 3.45 and 3.21 eV, respectively, while the ΔG of the last two steps are comparatively small, being −1.77 and 0.03 eV, respectively. Although the additional energy provided by photo-
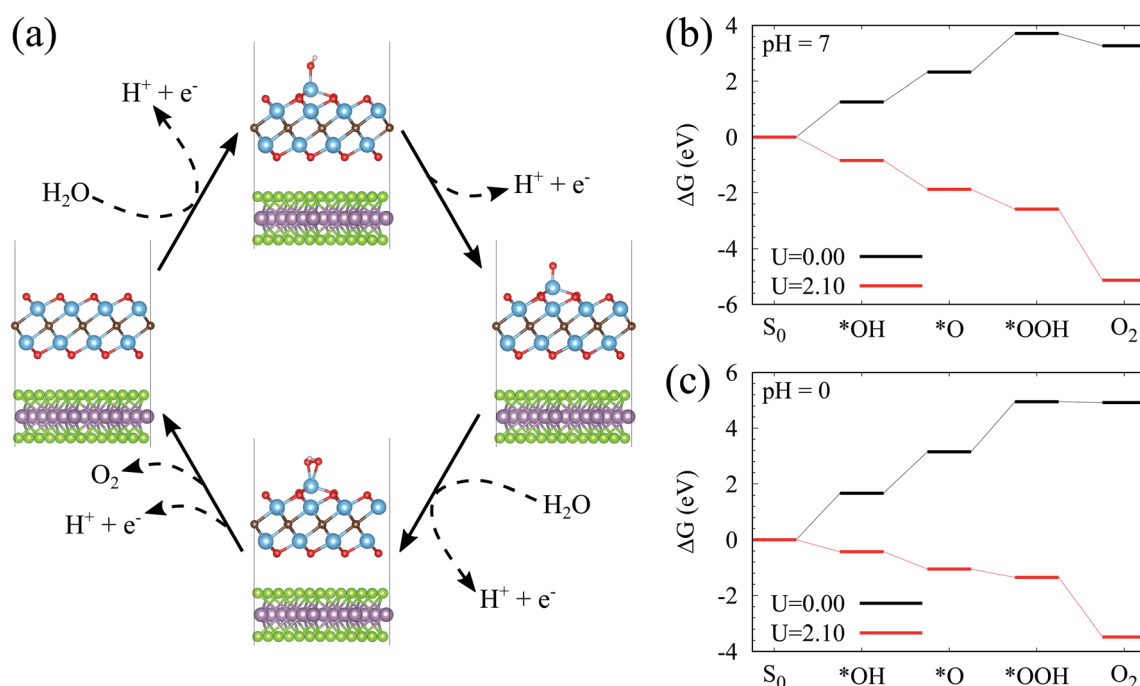

Fig. 3 (a) Proposed photocatalytic pathways for the OER on the surface of Ti_2CO_2. (b and c) Free energy diagrams for the OER on the surface of Ti_2CO_2 at pH = 7 and pH = 0, respectively.
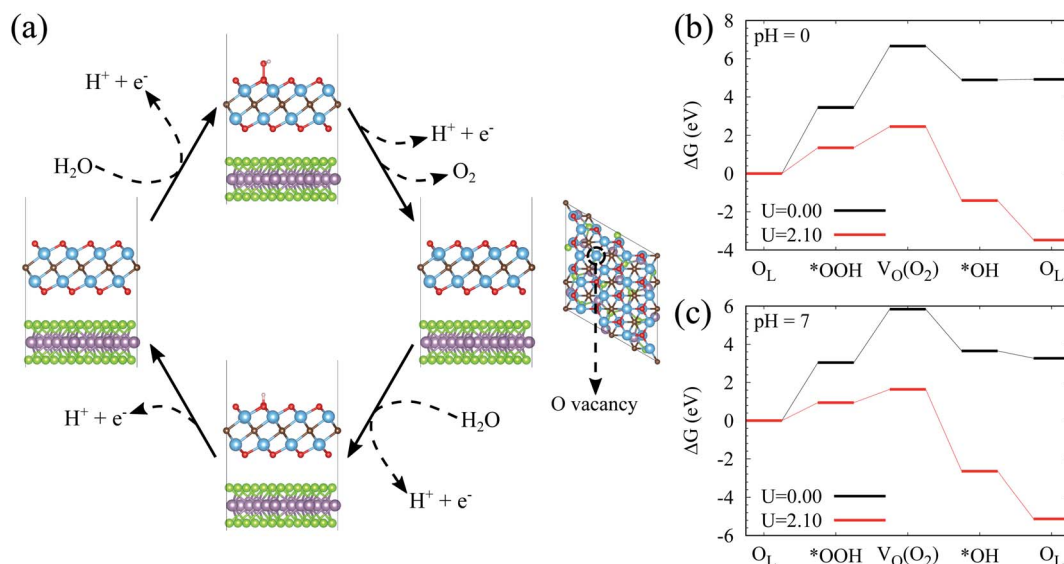
Fig. 4 (a) Proposed reaction pathways for the surface lattice O of Ti$_2$CO$_2$ oxidized by photo-generated holes. (b and c) Free energy diagrams for the oxidation of the surface lattice O for Ti$_2$CO$_2$ at pH = 0 and pH = 7, respectively.

generated holes is considered, ΔG of the first two steps is still higher than 1.10 eV, uncovering the fact that it is difficult for O$_L$ joining in the OER to generate O$_2$. However, the ΔG of the last two steps tend to be negative, indicating that the surface V$_O$ of Ti$_2$CO$_2$ easily reacts with H$_2$O molecules to recover the perfect surface morphology. According to the OER free energy changes,

it can be reasonably concluded that Ti$_2$CO$_2$ features promising corrosion resistance to the photo-generated holes. When the pH value increases to 7, Ti$_2$CO$_2$ still shows good anti-photocorrosion (Fig. 4(c)).

Light absorption is a crucial indicator to assess photocatalysts. The light absorption spectra of the MoSe$_2$ and Ti$_2$CO$_2$ monolayers as well as the MoSe$_2$/Ti$_2$CO$_2$ heterojunction are presented in Fig. 5(a). The preferable light absorption region for the MoSe$_2$ monolayer locates in the scope of visible and ultraviolet light. Benefiting from the smaller band gap of the Ti$_2$CO$_2$ monolayer, its light absorption can extend into the near-infrared light region. Accordingly, the MoSe$_2$/Ti$_2$CO$_2$ heterojunction demonstrates promising light absorption in the near-infrared, visible and ultraviolet light areas, indicative of the high STH efficiency. Referring to the previous work,[27,46] we calculated the STH efficiency of the MoSe$_2$/Ti$_2$CO$_2$ complex. The up limit of the theoretically predicted STH efficiency is as high as 12% (Fig. 5(b)), which is higher than the theoretical predictions of 10.5% and 9.3% for the Z-scheme photocatalysts of MoSe$_2$/SnSe$_2$ and WSe$_2$/SnSe$_2$,[27] respectively, and comparable to the experimentally reported efficiency of 13% gained in dye-sensitized solar cells.[47] Moreover, the predicted STH efficiency exceeds the required criterion of 10% for commercial applications,[37] which makes it a promising photocatalyst candidate for hydrogen production.
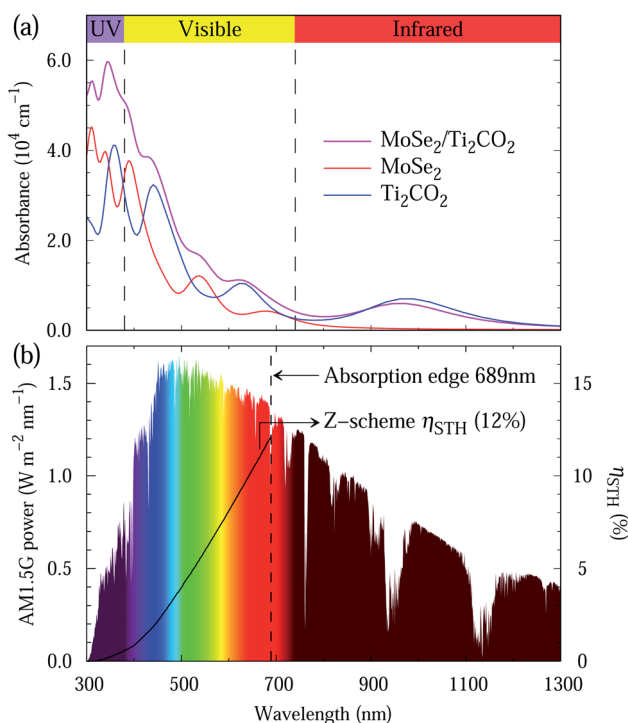
Conclusions

In summary, by employing first-principles calculations, we firstly construct a 2D vdW MoSe$_2$/Ti$_2$CO$_2$ heterojunction that has resistance to both electron–hole recombination and photocorrosion existing in the 2D TMD family for photocatalytic water splitting. The 2D MoSe$_2$/Ti$_2$CO$_2$ heterojunction is demonstrated to be a direct Z-scheme photocatalyst for overall

Fig. 5 (a) Calculated optical absorption spectra of the free-standing MoSe$_2$ and Ti$_2$CO$_2$ monolayers as well as the MoSe$_2$/Ti$_2$CO$_2$ heterojunction. (b) AM1.5G solar energy power density and theoretically predicted solar-to-hydrogen efficiency at 100% quantum efficiency.

water splitting. The HER and OER proceed on the surfaces of $MoSe_2$ and Ti_2CO_2, respectively, which is favourable for electron–hole separation. NAMD simulations reveal that over 65% of the photo-generated holes migrate from $MoSe_2$ to Ti_2CO_2 within 0.5 ps, which effectively brings down the possibility of photocorrosion in $MoSe_2$ caused by the photo-generated holes. The free energy variations along the OER pathway confirm that the OER occurs spontaneously on the Ti_2CO_2' surface under light irradiation. Meanwhile, the exorbitant free energy rises suppress the Ti_2CO_2' surface lattice O oxidized by the photo-generated holes, bringing about promising anti-photocorrosion. The $MoSe_2/Ti_2CO_2$ heterojunction shows good light absorption in the regions of the near-infrared, visible and ultraviolet light, thus resulting in a high STH efficiency of 12%. Such efficiency outperforms the 10% critical value, indicating the substantial potential of the $MoSe_2/Ti_2CO_2$ heterojunction for commercial applications. The concept proposed in this work can be further extended to other 2D laminates, to further alleviate the occurrence of photocorrosion for sulfide-, nitride-, and phosphide-based photocatalysts.

Conflicts of interest

The authors declare no conflict of interest.

Acknowledgements

References

1 G. Liu, C. Zhen, Y. Kang, L. Wang and H.-M. Cheng, *Chem. Soc. Rev.*, 2018, **47**, 6410–6444.

2 T. Su, Q. Shao, Z. Qin, Z. Guo and Z. Wu, *ACS Catal.*, 2018, **8**, 2253–2276.

3 M. Faraji, M. Yousefi, S. Yousefzadeh, M. Zirak, N. Naseri, T. H. Jeon, W. Choi and A. Z. Moshfegh, *Energy Environ. Sci.*, 2019, **12**, 59–95.

4 Y. Zhao, S. Zhang, R. Shi, G. I. N. Waterhouse, J. Tang and T. Zhang, *Mater. Today*, 2020, **34**, 78–91.

5 C.-F. Fu, X. Wu and J. Yang, *Adv. Mater.*, 2018, **30**, 1802106.

6 C.-F. Fu, C. Zhao, Q. Zheng, X. Li, J. Zhao and J. Yang, *Sci. China Chem.*, 2020, **63**, 1134–1141.

7 R. Lv, J. A. Robinson, R. E. Schaak, D. Sun, Y. Sun, T. E. Mallouk and M. Terrones, *Acc. Chem. Res.*, 2015, **48**, 56–64.

8 H. Li, C. Tsai, A. L. Koh, L. Cai, A. W. Contryman, A. H. Fragapane, J. Zhao, H. S. Han, H. C. Manoharan, F. Abild-Pedersen, J. K. Nørskov and X. Zheng, *Nat. Mater.*, 2016, **15**, 48–53.

9 Z. Li, X. Meng and Z. Zhang, *J. Photochem. Photobiol. C Photochem. Rev.*, 2018, **35**, 39–55.

10 S. Chandrasekaran, L. Yao, L. Deng, C. Bowen, Y. Zhang, S. Chen, Z. Lin, F. Peng and P. Zhang, *Chem. Soc. Rev.*, 2019, **48**, 4178–4280.

11 A. B. Ellis, S. W. Kaiser, J. M. Bolts and M. S. Wrighton, *J. Am. Chem. Soc.*, 1977, **99**, 2839–2848.

12 J. Su, Y. Wei and L. Vayssieres, *J. Phys. Chem. Lett.*, 2017, **8**, 5228–5238.

13 B. Weng, M.-Y. Qi, C. Han, Z.-R. Tang and Y.-J. Xu, *ACS Catal.*, 2019, **9**, 4642–4687.

14 E. Parzinger, B. Miller, B. Blaschke, J. A. Garrido, J. W. Ager, A. Holleitner and U. Wurstbauer, *ACS Nano*, 2015, **9**, 11302–11309.

15 H. Wang, L. Zhang, Z. Chen, J. Hu, S. Li, Z. Wang, J. Liu and X. Wang, *Chem. Soc. Rev.*, 2014, **43**, 5234–5244.

16 J. Low, J. Yu, M. Jaroniec, S. Wageh and A. A. Al-Ghamdi, *Adv. Mater.*, 2017, **29**, 1601694.

17 Y. Wang, H. Suzuki, J. Xie, O. Tomita, D. J. Martin, M. Higashi, D. Kong, R. Abe and J. Tang, *Chem. Rev.*, 2018, **118**, 5201–5241.

18 K. Iwashina, A. Iwase, Y. H. Ng, R. Amal and A. Kudo, *J. Am. Chem. Soc.*, 2015, **137**, 604–607.

19 S. Wang, B. Y. Guan, Y. Lu and X. W. Lou, *J. Am. Chem. Soc.*, 2017, **139**, 17305–17308.

20 J. Zhang, Y. Guo, Y. Xiong, D. Zhou and S. Dong, *J. Catal.*, 2017, **356**, 1–13.

21 R. Kumar, D. Das and A. K. Singh, *J. Catal.*, 2018, **359**, 143–150.

22 C. He, J. H. Zhang, W. X. Zhang and T. T. Li, *J. Phys. Chem. Lett.*, 2019, **10**, 3122–3128.

23 B. Gao, J.-R. Zhang, L. Chen, J. Guo, S. Shen, C.-T. Au, S.-F. Yin and M.-Q. Cai, *Appl. Surf. Sci.*, 2019, **492**, 157–165.

24 Y. Yao, J. Cao, W. Yin, L. Yang and X. Wei, *J. Phys. D: Appl. Phys.*, 2019, **53**, 55108.

25 C.-F. Fu, Q. Luo, X. Li and J. Yang, *J. Mater. Chem. A*, 2016, **4**, 18892–18898.

26 C.-F. Fu, R. Zhang, Q. Luo, X. Li and J. Yang, *J. Comput. Chem.*, 2019, **40**, 980–987.

27 Y. Fan, J. Wang and M. Zhao, *Nanoscale*, 2019, **11**, 14836–14843.

28 Z. Zhou, X. Niu, Y. Zhang and J. Wang, *J. Mater. Chem. A*, 2019, **7**, 21835–21842.

29 J. Low, C. Jiang, B. Cheng, S. Wageh, A. A. Al-Ghamdi and J. Yu, *Small Methods*, 2017, **1**, 1700080.

30 J. Pang, R. G. Mendes, A. Bachmatiuk, L. Zhao, H. Q. Ta, T. Gemming, H. Liu, Z. Liu and M. H. Rummeli, *Chem. Soc. Rev.*, 2019, **48**, 72–133.

31 J. Peng, X. Chen, W.-J. Ong, X. Zhao and N. Li, *Chem*, 2019, **5**, 18–50.

32 M. Naguib, V. N. Mochalin, M. W. Barsoum and Y. Gogotsi, *Adv. Mater.*, 2014, **26**, 992–1005.

33 M. Naguib, O. Mashtalir, J. Carle, V. Presser, J. Lu, L. Hultman, Y. Gogotsi and M. W. Barsoum, *ACS Nano*, 2012, **6**, 1322–1331.

34 M. Zhu, Z. Sun, M. Fujitsuka and T. Majima, *Angew. Chem., Int. Ed.*, 2018, **57**, 2160–2164.

35 L. Wang, X. Zheng, L. Chen, Y. Xiong and H. Xu, *Angew. Chem., Int. Ed.*, 2018, **57**, 3454–3458.

36 Q. Xu, B. Zhu, C. Jiang, B. Cheng and J. Yu, *Sol. RRL*, 2018, **2**, 1800006.

37 C. R. Cox, J. Z. Lee, D. G. Nocera and T. Buonassisi, *Proc. Natl. Acad. Sci.*, 2014, **111**, 14057–14061.

38 M. Khazaei, M. Arai, T. Sasaki, C.-Y. Chung, N. S. Venkataramanan, M. Estili, Y. Sakka and Y. Kawazoe, *Adv. Funct. Mater.*, 2013, **23**, 2185–2192.

39 Y. Xie and P. R. C. Kent, *Phys. Rev. B: Condens. Matter Mater. Phys.*, 2013, **87**, 235441.

40 Y. Chen, T. Shi, P. Liu, X. Ma, L. Shui, C. Shang, Z. Chen, X. Wang, K. Kempa and G. Zhou, *J. Mater. Chem. A*, 2018, **6**, 19167–19175.

41 B. V Lotsch, *Annu. Rev. Mater. Res.*, 2015, **45**, 85–109.

42 Y. Liu, N. O. Weiss, X. Duan, H.-C. Cheng, Y. Huang and X. Duan, *Nat. Rev. Mater.*, 2016, **1**, 16042.

43 R. Zhang, L. Zhang, Q. Zheng, P. Gao, J. Zhao and J. Yang, *J. Phys. Chem. Lett.*, 2018, **9**, 5419–5424.

44 Q. Zheng, W. Chu, C. Zhao, L. Zhang, H. Guo, Y. Wang, X. Jiang and J. Zhao, *Wiley Interdiscip. Rev. Comput. Mol. Sci.*, 2019, **9**, e1411.

45 X. Niu, X. Bai, Z. Zhou and J. Wang, *ACS Catal.*, 2020, **10**, 1976–1983.

46 C.-F. Fu, J. Sun, Q. Luo, X. Li, W. Hu and J. Yang, *Nano Lett.*, 2018, **18**, 6312–6317.

47 S. Mathew, A. Yella, P. Gao, R. Humphry-Baker, B. F. E. Curchod, N. Ashari-Astani, I. Tavernelli, U. Rothlisberger, M. K. Nazeeruddin and M. Grätzel, *Nat. Chem.*, 2014, **6**, 242–247.